Modeling metastabilities in chalcopyrite-based thin film solar cells

Koen Decock, Paweł Zabierowski, and Marc Burgelman

Citation: J. Appl. Phys. **111**, 043703 (2012); doi: 10.1063/1.3686651
View online: http://dx.doi.org/10.1063/1.3686651
View Table of Contents: http://jap.aip.org/resource/1/JAPIAU/v111/i4
Published by the American Institute of Physics.

Modeling metastabilities in chalcopyrite-based thin film solar cells

Koen Decock,[1,a)] Paweł Zabierowski,[2] and Marc Burgelman[1]
[1]*Department of Electronics and Information Systems (ELIS), University of Gent, St- Pietersnieuwstraat 41, B-9000 Gent, Belgium*
[2]*Faculty of Physics, Warsaw University of Technology, Koszykowa 75, Warszawa 00 662, Poland*

(Received 28 September 2011; accepted 24 January 2012; published online 21 February 2012)

$Cu(In,Ga)Se_2$-based thin film solar cell devices exhibit metastable electrical behavior. This behavior is often ascribed to intrinsic defects that can change configuration accompanied by large lattice relaxations. We extended the thin film solar cell simulation software SCAPS to enable the simulation of the metastable behavior of this kind of defects. The statistics that are needed to describe metastable defects are discussed. The procedure that has been implemented is introduced, and special attention is paid to the convergence of the method for high defect densities. The model is demonstrated by simulating the effect of voltage induced metastabilities on the capacitance-voltage characteristics. Some of the features present in the measured apparent doping density profiles can be directly related to presence of metastable defects. © *2012 American Institute of Physics*. [doi:10.1063/1.3686651]

INTRODUCTION

Metastable changes in the electrical characteristics of $Cu(In,Ga)Se_2$ (CIGS)-based thin-film solar cells have been investigated for many years.[1–4] Several models have been proposed to explain these metastabilities.[5–8] First principle calculations[9,10] show that the trapping of carriers at the intrinsic defects V_{Se}, In_{Cu}, and Ga_{Cu} and their complexes with the copper vacancy V_{Cu} is accompanied by large lattice relaxations. Relating the metastabilities to the lattice relaxations in V_{Se} and In_{Cu} defects is one of the most plausible explanations. A convincing method to verify whether the presence of defects with lattice relaxations can explain the observed metastable effects is to perform numerical simulations. Several attempts have been undertaken to mimic the effect of such lattice relaxations by introducing additional charge in a specified region of the absorber layer.[11,12] Different metastable states are then modeled by changing the width of this region.

The numerical simulation program SCAPS[13] has been designed to simulate CIGS and CdTe-based thin film solar cell devices. It is able to model general multivalent defects.[14] We extended this software to be able to simulate the metastabilities predicted for V_{Se} and In_{Cu} defects in CIGS.

These metastable defects are considered to exist in two different configurations, a donor and an acceptor configuration, which are separated by energy barriers associated with lattice relaxations. Each separate configuration behaves as a conventional defect, which can have a multivalent character. The transition between the different configurations requires a simultaneous capture or emission of two free carriers together with thermal activation over an energy barrier. Hence, at lower temperatures, this transition will not occur. Similarly the transition will not be observed in an admittance measurement when the change of the quasi-Fermi levels occurs at higher frequencies.

In a typical experiment, the studied sample is brought to a well defined metastable state, i.e., a distribution over the donor and acceptor configuration, by applying certain initial voltage/illumination conditions at elevated temperatures ($T > 300$ K) for a sufficiently long time. Afterward the sample is cooled down to inhibit further changes in the metastable state of the sample and measurements are performed. To simulate this, first the distribution over the acceptor and donor configuration of the defect is calculated under initial voltage/illumination conditions. This distribution, together with the total defect density, is used to calculate the defect density belonging to the different configurations of the metastable defect. These calculated defect densities are then used to perform further simulations.

In a first section, the statistics governing the transition between the different configurations is discussed. Afterward, the algorithm that has been implemented to calculate the metastable charge and defect distribution is introduced. When the defect density is high with respect to the shallow doping density, the convergence of this algorithm has to be improved using a clamping technique. The implemented model is finally demonstrated by simulating the effect of voltage induced metastabilities on the capacitance-voltage characteristics of thin film CIGS-based solar cells. The model proposed by Kimerling[15] to analyze the effect of deep traps on the apparent doping density profiles has been extended to explain specific features of the capacitance-voltage measurements and simulations.

Statistics of the donor/acceptor conversion of metastable defects

Every transition process between the different configurations of a metastable defect requires a simultaneous capture or emission of two free carriers together with thermal activation over an energy barrier, and has a specific transition rate τ^{-1}. A general transition, involving m different capture/emission processes Px, can be described according to Eq. (1).

a)Author to whom correspondence should be addressed. Electronic mail: Koen.Decock@elis.ugent.be.

$$\tau^{-1} = \nu_{ph} \exp\left(-\frac{\Delta E}{k_B T}\right) \prod_{x=1}^{m} \frac{\tau_{Px}^{-1}}{\nu_{ph}} \tag{1}$$

with ν_{ph} the phonon frequency and ΔE the energy barrier associated with the process. T represents the temperature and k_B is Boltzmann's constant. τ_{Px}^{-1} is the transition rate associated with a single capture or emission process. These transition rates are given by

$$\begin{aligned} \tau_{ec}^{-1} &= c_n n = c_n N_C \exp\left(\frac{E_{Fn} - E_C}{k_B T}\right) \\ \tau_{ee}^{-1} &= c_n N_C \\ \tau_{hc}^{-1} &= c_p p = c_p N_V \exp\left(\frac{E_V - E_{Fp}}{k_B T}\right) \\ \tau_{he}^{-1} &= c_p N_V. \end{aligned} \tag{2}$$

The first subscript indicates an electron (e) or hole (h) process, the second a capture (c) or emission (e) process. N_C and N_V are the effective density of states in the conduction and valence band, E_C and E_V are the conduction and valence band energies, and E_{Fn} and E_{Fp} are the quasi-Fermi level energies for electrons and holes. The electron and hole densities are denoted by n and p, and the capture constants by c_n and c_p. Limited to transitions governed by only two simultaneous capture/emission processes, Eq. (1) reduces to Eq. (3).

$$\tau^{-1} = \frac{1}{\nu_{ph}} \tau_{P1}^{-1} \tau_{P2}^{-1} \exp\left(-\frac{\Delta E}{k_B T}\right). \tag{3}$$

The transition between the donor and acceptor configuration is assumed to be possible via four different processes: hole capture (HC), electron capture (EC), hole emission (HE), and electron emission (EE). Each of these processes consists out of two simultaneous single capture/emission processes. Considering, e.g., the (V_{Se}–V_{Cu}) complex,[9] the HC process is shown in Eq. (4) and the EC process in Eq. (5).

$$(V_{Se} - V_{Cu})^{-} + 2h \rightarrow (V_{Se} - V_{Cu})^{+} \tag{4}$$

$$(V_{Se} - V_{Cu})^{+} + e \rightarrow (V_{Se} - V_{Cu})^{-} + h. \tag{5}$$

Note that there are more than four different processes possible, e.g., the EC process (5) can proceed through double electron capture as well. However, the energy barriers associated with these additional processes are much higher so that they can be neglected in the temperature interval which is usually studied.[9] At very high temperatures ($T > 400$ K), other processes can gain importance. The emission processes are considered to be the inverse process of the corresponding capture process. This implies that the HE and EE processes for the (V_{Se}–V_{Cu}) complex are found by switching the direction of the arrow in Eqs. (4) and (5).

The interplay of the different transition processes will lead to a steady state distribution of the donor and acceptor configuration, which is dependent of the position of the (quasi-) Fermi levels and the temperature. The Fermi level position where the donor and acceptor configuration are equally stable under thermal equilibrium conditions is called the *transition energy*[9] and will be noted as E_{TR}.

The activation energies related to the different processes together with the transition energy are not independent because the expressions (3) should obey the principle of detailed balance. Under thermal equilibrium, the capture and emission processes oppose each other, there is no net recombination and the distribution over the configurations remains constant. When the Fermi level position equals the transition energy, the relations shown in Eq. (6) are valid.

$$\begin{cases} \tau_{EC}^{-1} = \tau_{EE}^{-1} \\ \tau_{HC}^{-1} = \tau_{HE}^{-1} \end{cases}. \tag{6}$$

This leads to two relations that should hold for the five unknown energy values: ΔE_{EC}, ΔE_{EE}, ΔE_{HE}, ΔE_{HC}, E_{TR}. Hence, only three of them are independent. Considering the (V_{Se}–V_{Cu}) complex, see Eqs. (4) and (5), Eq. (6) can be rewritten as Eq. (7).

$$\begin{cases} E_{TR} - E_C - \Delta E_{EC} = -\Delta E_{EE} + E_V - E_{TR} \\ 2E_V - 2E_{TR} - \Delta E_{HC} = -\Delta E_{HE}. \end{cases} \tag{7}$$

Specific details for V_{Se} and In_{Cu} complexes

The reactions of the capture processes for the (V_{Se}–V_{Cu}) complex are shown in Eqs. (4) and (5). For the In_{Cu} complexes, the HC process exhibits a similar reaction path as Eq. (4), the EC process, however, follows the reaction shown in Eq. (8).

$$(In_{Cu} - V_{Cu})^{+} + 2e \rightarrow (In_{Cu} - V_{Cu})^{-}. \tag{8}$$

Most values for the activation and transition energies have been calculated from first principle calculations by Lany and Zunger.[9,10] It can easily be checked that those values obey the detailed balance principle. Table I gives an overview of these energy values together with additional values calculated using detailed balance considerations.

TABLE I. Overview of the transition energies given by Lany and Zunger (Refs. 9, 10) completed using detailed balance calculations (marked with *). When no value for either ΔE_{EC} or ΔE_{EE} is given, it cannot be calculated using detailed balance considerations either. The activation energy for the HC process is chosen 0.0 as the DX state is immediately emptied in the presence of free holes (Ref. 10).

	E_{TR} (eV)	ΔE_{EC} (eV)	ΔE_{HC} (eV)	ΔE_{EE} (eV)	ΔE_{HE} (eV)
			$CuInSe_2$ ($E_g = 1.04$ eV)		
(V_{Se}–V_{Cu})	0.19	0.1	0.35	0.76	0.73
In_{Cu}	0.92	0.08*	0.0	0.32	1.84*
(In_{Cu}–V_{Cu})	1.11	—	0.0	—	2.22*
(In_{Cu}–$2V_{Cu}$)	1.30	—	0.0	—	2.60*
			$CuGaSe_2$ ($E_g = 1.68$ eV)		
(V_{Se}–V_{Cu})	0.32	0.0	0.28	1.04*	0.92
Ga_{Cu}	0.84	—	0.0	—	1.68*
(Ga_{Cu}–V_{Cu})	1.02	—	0.0	—	2.04*
(Ga_{Cu}–$2V_{Cu}$)	1.36	—	0.0	—	2.72*

Correspondence with conventional single capture/emission processes

Considering the transition of a certain state to consist of a single carrier process, the conventional emission constants can be obtained. In this case, the capture processes are not thermally activated: $\Delta E_{EC} = \Delta E_{HC} = 0.0\,\text{eV}$, and the transition energy E_{TR} is the defect level energy E_t. Detailed balance calculations lead then to $\Delta E_{EE} = E_C - E_t$ and $\Delta E_{HE} = E_t - E_V$. Substitution in Eqs. (1) and (2) leads to $\tau_{HC}^{-1} = \tau_{hc}^{-1} = c_p p$, $\tau_{EC}^{-1} = \tau_{ec}^{-1} = c_n n$, $\tau_{HE}^{-1} = \tau_{he}^{-1} \times \exp[-(E_t - E_V)/k_B T] = e_p$, and $\tau_{EE}^{-1} = \tau_{ee}^{-1} \times \exp[-(E_C - E_t)/k_B T] = e_n$.

Numerical solution method

For notational convenience, we will consider the transition (+/−) between the donor configuration D^+ and the acceptor configuration A^-. The total density of the metastable defect is noted as N_t. The fraction of defects in the acceptor configuration is given by f_A, the fraction in the donor configuration by f_D, with $f_D + f_A = 1$. Each configuration of the defect acts as a conventional defect. The fraction of defects belonging to a certain configuration that is in charge state s, is given by f_t^s. The number of defects in the acceptor configuration, which is negatively charged, is then given by $f_{t,A}^- \times f_A \times N_t$. The transition rates U from donor to acceptor and acceptor to donor are then given by Eq. (9).

$$\begin{aligned} U_{A^- \to D^+} &= f_{t,A}^- f_A \left(\tau_{EE}^{-1} + \tau_{HC}^{-1}\right) N_t \\ U_{D^+ \to A^-} &= f_{t,D}^+ f_D \left(\tau_{HE}^{-1} + \tau_{EC}^{-1}\right) N_t. \end{aligned} \tag{9}$$

Under steady state conditions, these rates are equal. Taking into account $f_D + f_A = 1$, the distribution over donor and acceptor configuration can be calculated (Eq. (10)).

$$\begin{aligned} f_A &= \frac{f_{t,D}^+ \left(\tau_{HE}^{-1} + \tau_{EC}^{-1}\right)}{f_{t,D}^+ \left(\tau_{HE}^{-1} + \tau_{EC}^{-1}\right) + f_{t,A}^- \left(\tau_{EE}^{-1} + \tau_{HC}^{-1}\right)} \\ f_D &= \frac{f_{t,A}^- \left(\tau_{EE}^{-1} + \tau_{HC}^{-1}\right)}{f_{t,D}^+ \left(\tau_{HE}^{-1} + \tau_{EC}^{-1}\right) + f_{t,A}^- \left(\tau_{EE}^{-1} + \tau_{HC}^{-1}\right)}. \end{aligned} \tag{10}$$

Because the values of f_A and f_D influence the charge distribution and thus the quasi-Fermi level position, they influence f_t^s and the time constants that are present in Eq. (10) as well. As a result, the metastable configuration distribution has to be calculated in an iterative way. As a starting point, the electrostatic potential and the quasi-Fermi level positions are calculated assuming the configuration distribution to be constant throughout the sample, e.g., $f_A = f_D = [0.5]$. In the first iteration step, the resulting values of f_t^s and τ^{-1} are used to update the values of f_A and f_D according to Eq. (10). In turn, these updated values lead to a recalculation of the potential and the quasi-Fermi level positions and thus to updated values of f_t^s and τ^{-1} again. With these new values, the next iteration step can be performed. The iteration procedure continues as long as the maximal relative difference between the previous and the updated values of f_A, f_D, and f_t^s is larger than a predefined tolerance.

Clamping

Straightforward application of this iteration scheme can lead to divergence due to overcompensation, especially when the defect density is higher than the shallow doping density. The origin of this divergence in this case is the fact that the updating of f_A and f_D and of the Fermi level position has an opposite effect. When the updating of f_A and f_D leads to an increased acceptor concentration (f_A increases), more negative space charge will be present in the structure; this will lead to a lowering of the Fermi level position. In turn, this lowering will lead to a decreased acceptor concentration (f_A decreases). If the defect density is large, one can get to a situation where the change in acceptor concentration in one iteration step is exactly opposite to the change in the previous step and much larger than the predefined tolerance. To circumvent this problem, the change in f_A and f_D has to be limited during the iteration procedure (*clamping*). This clamping is performed according to Eq. (11).

$$f_A = f_A^{old} \left(\frac{f_A^{new}}{f_A^{old}}\right)^x, \tag{11}$$

with f_A^{old} the value of f_A after the previous iteration step, f_A^{new} the value of f_A calculated according to Eq. (10) and $0 < x \leq 1$ the clamping factor. If $x = 1$, no clamping is present and $f_A = f_A^{new}$. A similar expression holds for the fraction of defects in the donor configuration. The clamping as given by Eq. (11) is applied to the smallest of f_A and f_D. The complementary fraction is then calculated according to $f_D + f_A = 1$. Straightforward application of the clamping procedure leads to a better convergence but does not give a correct solution yet as Eq. (10) is violated. The resulting solution after reaching the tolerance threshold while applying the clamping is, however, very close to the true solution. This solution is then used as an initial guess for an iteration cycle without clamping to get to the final solution of the system.

The problem of overcompensation will be circumvented more efficiently for smaller clamping values x. As a result, the algorithm will converge for higher defect density values. However, more iterations will be needed to get to the solution. The effect of x on the convergence of the algorithm is illustrated on a simple uniform structure, representing a solar cell consisting of a uniform absorber of $Cu(In_{0.8},Ga_{0.2})Se_2$. The shallow doping level in the absorber is $10^{16}\,\text{cm}^{-3}$, and a $(V_{Se}-V_{Cu})$ metastability is present. The calculations are performed with a tolerance of 10^{-6}. Figure 1 shows the number of iterations needed to get to convergence for varying defect density values. For high x values (close to one), this number increases fast for increasing defect density, for low x values, it is constant. When the clamping factor is decreased, both the number of iterations at low defect density and the minimum defect density at which divergence occurs increase. This is illustrated in more detail in Fig. 2. For small values of x, the number of iterations needed to get to convergence is in good approximation proportional to $x^{-0.93}$. The maximal defect density that leads to convergence increases fast with decreasing x and starts to saturate for $x < 0.05$.

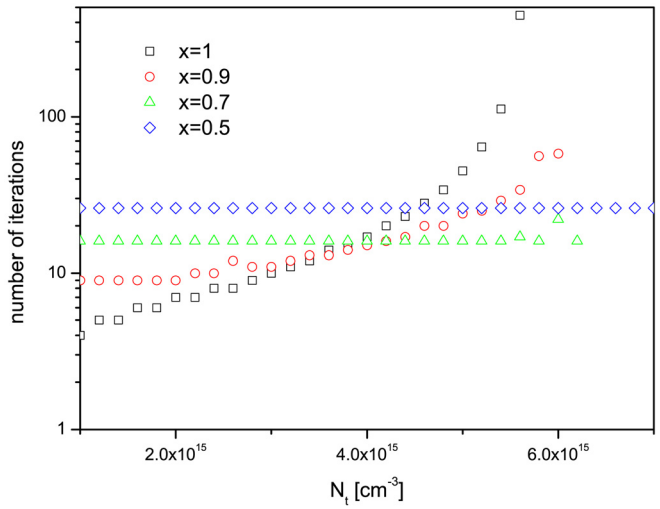

FIG. 1. (Color online) Number of iterations needed to get to convergence as a function of the defect density for different clamping factors. The curves are broken off at the defect density where divergence occurs.

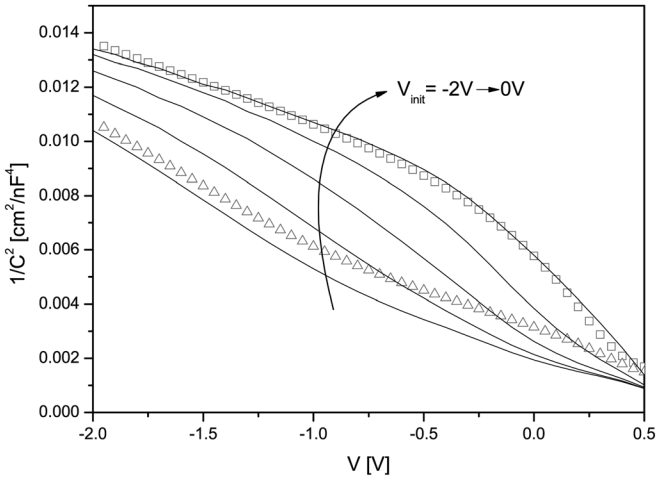

FIG. 3. Mott–Schottky plots of *C-V*-measurements ($T = 200$ K; $f = 1$ MHz) in the relaxed state (squares) and after reverse bias treatment (triangles). The reverse bias state was obtained by applying -2 V at 300 K for 1 h before measurement. The solid lines are the simulation results for different voltages applied during the reverse bias treatment (V_{init}) ranging from -2 V to 0 V in steps of 0.5 V.

RESULTS

The algorithm presented in the previous sections is now used to simulate the effect of reverse bias treatment on capacitance-voltage (*C-V*) measurements on CIGS-based solar cells. Applying a reverse bias at elevated temperatures before starting the measurements at low temperatures leads to a horizontal shift of the Mott–Schottky plots toward lower voltages.[11] Apparently, a reverse bias treatment results in an increase of the negative charge concentration close to the junction and a decrease farther away.[4] This effect is often ascribed to the presence of ($V_{Se}-V_{Cu}$) complexes.

The Mott–Schottky plots of *C-V*-measurements of a CIGS sample in the relaxed state and after a reverse bias treatment (1 h -2 V applied at 300 K) are shown in Fig. 3. The CIGS absorber layer of the sample has been grown on Mo coated soda lime glass substrates by thermal evaporation following the three stage process.[16] It has been finished with a 50 nm thick (CBD) CdS buffer and a 350 nm thick ZnO:Al window layer. We built a model that can mimic these measurements. To keep the structure as simple as possible, only three layers are introduced (window-buffer-absorber), and all parameters are assumed to be uniform. The parameters of the ($V_{Se}-V_{Cu}$) complex are based on the values calculated by Lany and Zunger[9] and are summarized in Table II. The shallow acceptor density is $N_A = 10^{15}$ cm^{-3}. An additional acceptor defect level at 0.33 eV above E_V with a defect density of $N_t = 1.4 \times 10^{16}$ cm^{-3} has been introduced as proposed in Ref. 12.

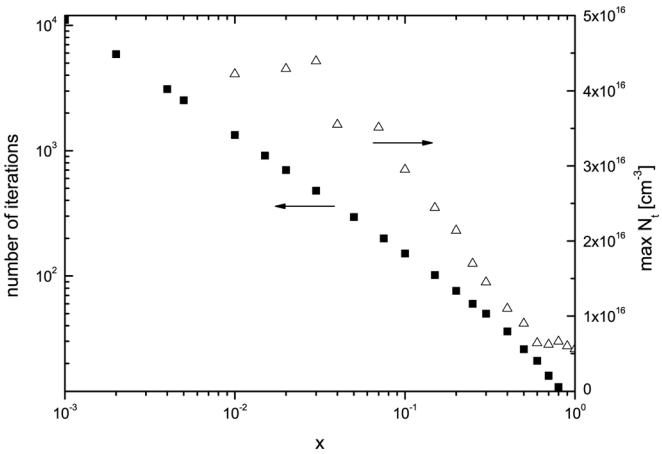

FIG. 2. Squares (left axis): Influence of the clamping factor on the number of iterations needed to get to convergence with a defect density of 2×10^{15} cm^{-3}. Triangles (right axis): Maximum defect density for which the algorithm converges as a function of the clamping factor. The tolerance is 10^{-6} and the maximum allowed number of iterations is 1000. The relative small increase of this maximum density (by a factor 8) is limited by the fact that for the ($V_{Se}-V_{Cu}$) complex, the metastable configuration distribution determines the free carrier density in the entire absorber at such high defect densities.

The simulations of the *C-V*-measurements of this structure are also shown in Fig. 3. The initial voltage (V_{init}), which is used to calculate the metastable configuration distribution, is varied from -2 V to 0 V in steps of 0.5 V. The simulations with $V_{init} = 0$ V and $V_{init} = -2$ V agree well with the measurements. The shape of the curves in between varies in a similar way as shown in Fig. 2 of Ref. 11. The corresponding apparent doping density is shown in Fig. 4. There is indeed an apparent increase of the negative charge concentration visible close to the interface. This increase is due to an increased fraction of ($V_{Se}-V_{Cu}$) complexes in the acceptor configuration (Fig. 5). When performing *C-V*

TABLE II. Overview of the parameters of the (V_{Se}–V_{Cu}) complex used in the simulations.

N_M (cm^{-3})	3×10^{15}	
ΔE_{TR} (eV)	0.25	
ΔE_{EC} (eV)	0.10	
ΔE_{HC} (eV)	0.35	
ΔE_{EE} (eV)	0.72	
ΔE_{HE} (eV)	0.85	
E_t (eV) above E_V	Acceptor configuration	Donor configuration
	0.85 (2 −/−) 0.06 (0/−)	1.00 (+/0)

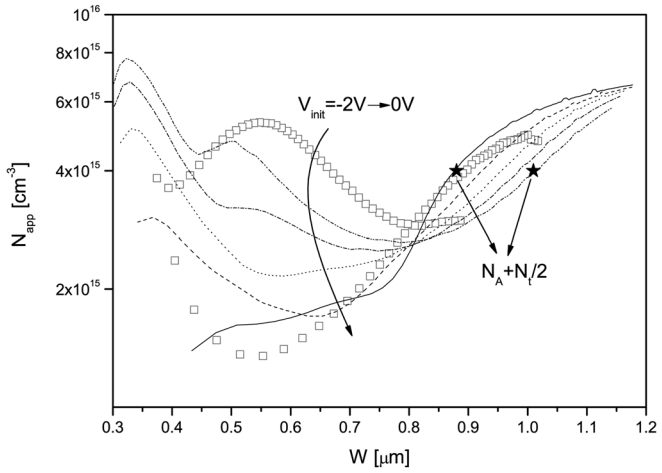

FIG. 4. Apparent defect density calculated from the *C-V* simulations ($T = 200\,\mathrm{K}$; $f = 1\,\mathrm{MHz}$; $V = -4\,\mathrm{V} \rightarrow 0.5\,\mathrm{V}$). The apparent defect density belonging to the measurement results displayed in Fig. 3 are shown using identical symbols. The stars mark the points where $N_{meas} \approx N_A + N_t/2$ and thus where $W = 2\,k$, as will be explained in the discussion section.

simulations in the voltage range from $-2\,\mathrm{V}$ to $0.5\,\mathrm{V}$, there is a decrease in the apparent doping density at larger distances from the interface. Increasing the voltage range to $-4\,\mathrm{V}$, however, shows that this decrease is the result of a horizontal shift of the minimum of the curve for more negative values of V_{init}.

It should be emphasized that the agreement between the simulation and measurement results has been obtained using a very simple model, and optimizing only a limited number of parameters. The properties of the ($V_{Se}-V_{Cu}$) complex as given in Ref. 9 for $CuInSe_2$ have been used, allowing for a variation between the values calculated using image charge correction or not. Only the value of E_{TR} has slightly been increased to 0.25 eV, see following text, which also influences the value of ΔE_{EE} and ΔE_{HE}.

To get to a good agreement with the measurement results, five parameters have been optimized: E_{TR}, the shallow doping density N_A, the ($V_{Se}-V_{Cu}$) complex density N_M, the density N_t of the additional acceptor defect and its energy E_t. The value of E_{TR} is crucial. E_{TR} does not only influence the position where the occupation of the acceptor configuration drops, it also influences the space charge in the bulk of the absorber because the occupation of the acceptor configuration does not drop to zero in the bulk. The reason for this is the fact that the transition energy of the ($V_{Se}-V_{Cu}$) complex is close to the Fermi level position in the bulk of the absorber. As a result there is a strong interdependence among E_{TR}, the shallow doping density and the metastable defect density. Because E_{TR} is not close to E_V for the In_{Cu} complexes, the importance of the E_{TR} there would not be as far reaching as for the ($V_{Se}-V_{Cu}$) complex. The shallow doping density influences the space charge density in the bulk of the absorber and thus also the slope of the Mott–Schottky diagram. The metastable defect density N_M also influences the space charge density in the bulk of the absorber in a similar way as the shallow doping density. Moreover, it influences the difference between the simulation results for different values of V_{init} and thus the splitting of the Mott–Schottky curves for $V_{init} = 0\,\mathrm{V}$ and $V_{init} = -2\,\mathrm{V}$. Optimization of the combination of the values of E_{TR}, N_A, and N_M is the key factor to get to a good agreement with the *C-V* measurement results. Nevertheless, there is still a minor influence of the defect density and energy of the additional acceptor defect. The presence of this defect is required to reproduce the increase of the apparent doping density for increasing values of W. In contrast to the other three parameters, the tolerance on the properties of this defect is larger. Its defect density can be lowered with a factor 5 without resulting in an obvious mismatch between measurement and simulation results.

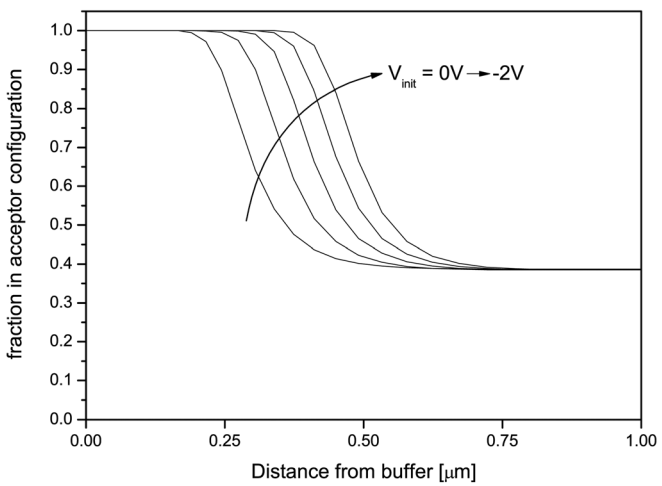

FIG. 5. Fraction of the ($V_{Se} - V_{Cu}$) complexes in the acceptor configuration.

The reverse bias treatment also influences the current-voltage characteristics of a CIGS-based solar cell. A decrease in fill factor and a roll over effect is observed at low temperatures.[2] There are several possible explanations for this behavior, the most important of them have been surveyed in Ref. 17. The rollover effect can be explained in terms of a back contact barrier, the presence of acceptor states at the buffer/window interface or a positive conduction band offset at the buffer/window interface. A reduced fill factor due to a kink in the current voltage characteristics can be explained by a positive conduction band offset at the absorber/buffer/window interfaces, a p^+ layer at the absorber front surface, or a conduction band grading at the absorber surface. The characteristics of these phenomena can be altered by a change of the distribution of the metastable defect configurations. The model that has been constructed to mimic the *C-V* measurement results is a very simple one, none of the abovementioned phenomena has been introduced yet. Due to the simplicity of the model, however, the introduction of these effects would not lead to insurmountable problems although they complicate the structure significantly.

DISCUSSION

Apparent doping density with deep traps and metastable charge

Kimerling[15] developed a model that explains the influence of deep traps on the measurement of the apparent doping density profiles. This model is based on a staircase

function (see Fig. 6) assuming deep traps to contribute to the space charge in a region with width y. Assuming an n^+p junction with a uniform shallow acceptor doping density N_A, this model predicts the following relations:

$$y = W - \left(\frac{2\varepsilon}{q^2}\frac{E_t - E_F}{N_A}\right)^{1/2} = W - k \tag{12}$$

$$N_{meas}(W) = N_A + N_t\frac{y}{W} \tag{13}$$

with W the depletion width, ε the dielectric permittivity, q the elementary charge, E_t the defect energy of the deep trap center, and N_t its defect density. N_{meas} is the apparent doping density that would result from the C-V-measurement. Equation (13) is illustrated in the bottom of Fig. 6.

The most straightforward way to introduce the effect of a metastable defect is to assume that the shallow doping density is piecewise uniform by adding an additional term N_M to the shallow doping density, which is only present in a region with width x_M as shown in the top of Fig. 6. This width is, contrary to y, not determined by the measurement voltage, but only by the initial voltage. Application of the theory developed in Ref. 15 taking into account this additional acceptor density leads to the following formulas:

$$y = \frac{N_A W + N_M x_M}{N_A + N_M} - \left(\frac{2\varepsilon}{q^2}\frac{E_t - E_F}{N_A + N_M} - \frac{N_A N_M}{(N_A + N_M)^2}(W - x_M)^2\right)^{1/2} \tag{14}$$

$$y = W - \left(\frac{2\varepsilon}{q^2}\frac{E_t - E_F}{N_A + N_M}\right)^{1/2} \tag{15}$$

where Eqs. (14) and (17) (with $\Delta y/\Delta W$ given by Eq. (18)) hold when $y < x_M < W$, Eqs. (12) and (13) hold when $x_M < y < W$, and Eqs. (15) and (16) hold when $y < W < x_M$.

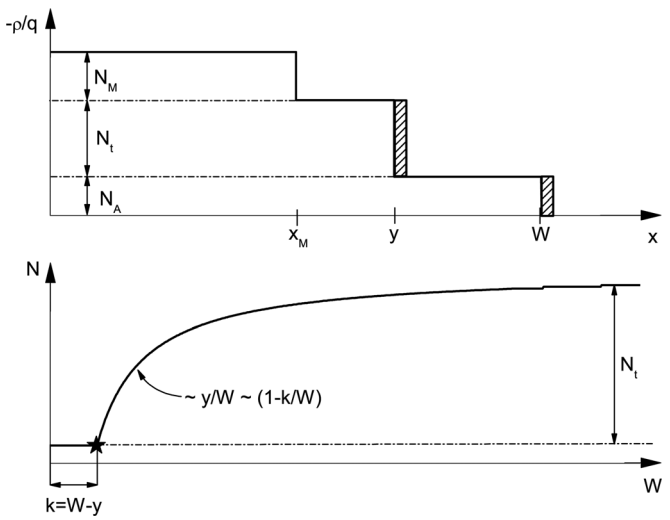

FIG. 6. Top: Staircase model for the acceptor density in the presence of a metastable defect density N_M. Bottom: Free-carrier profile as predicted by Kimerling Eq. (13) for a uniform acceptor density in the presence of a deep acceptor trap ($N_M = 0$ in this case). The point where $W = k$ is marked with a star.

$$N_{meas}(W) = N_A + N_M + N_t\frac{y}{W} \tag{16}$$

$$N_{meas}(W) = N_A + N_t\frac{y}{W}\frac{\Delta y}{\Delta W} \tag{17}$$

$$\frac{\Delta y}{\Delta W} = \frac{N_A}{N_A + N_M} + \frac{N_A N_M (W - x_M)}{(N_A + N_M)^2} \times \left(\frac{2\varepsilon_0\varepsilon}{q^2}\frac{E_t - E_F}{N_A + N_M} - \frac{N_A N_M (W - x_M)^2}{(N_A + N_M)^2}\right)^{-1/2}. \tag{18}$$

In all equations, N_t is assumed to be independent of the metastable state of the sample. However, when N_t would correspond to one of the configurations of the metastable defect, there will be an additional interdependence between N_t and the metastable state of the sample. This interdependence can not straightforwardly be introduced in the analytical model but needs to be investigated through full numerical simulations. In the example given, however, N_t can not be associated with one of the configurations of the metastable defect because $N_t > N_M$.

Application to the simulation results

The theory of the previous section can now be applied to the simulated and measured apparent doping density shown in Fig. 4. At large values of W, the apparent doping density increases. This can already be explained by the standard theory proposed by Kimerling as shown in Fig. 6. Two features, however, cannot be explained by this standard theory, as they rely on the inclusion of a metastable defect density N_M. When the initial voltage gets more reverse, a local maximum appears at $W \approx 0.5\ \mu$m, and the curves experience a horizontal translation at large values of W.

The parameters that have been used to obtain the full numerical model are substituted in the equations of the previous section: $N_A = 10^{15}\,\text{cm}^{-3}$, $N_M = 3 \times 10^{15}\,\text{cm}^{-3}$, $N_t = 1.4 \times 10^{16}\,\text{cm}^{-3}$, $E_t = 0.33\,\text{eV}$. The Fermi level energy is calculated as $E_F = k_B T \times \ln(N_V/N_A)$. Two situations are examined: $V_{init} = 0\,\text{V}$ leads to $x_M = 0.3\ \mu$m and $V_{init} = -2\,\text{V}$ leads to $x_M = 0.5\ \mu$m as can be seen in Fig. 5. The results are shown in Fig. 7 and correspond well with the measurement and simulation results.

In the W range displayed in Fig. 7, all three equations, (13), (16), and (17), are needed to calculate N_{meas} when $V_{init} = -2\,\text{V}$. Equation (16) is, however, redundant when $V_{init} = 0\,\text{V}$. As a result, a local maximum for N_{meas} occurs around $0.5\ \mu$m only when $V_{init} = -2\,\text{V}$. This maximum is created as follows. For $W < x_M$, y and N_{meas} are calculated using Eqs. (15) and (16), leading to a strong increase of N_{meas} for increasing W. At $W = x_M$, however, the applicable equations change to Eqs. (14) and (17), leading to a sharp drop of N_{meas}. This drop is further enhanced by a smaller decrease of N_{meas} with increasing W because y does not increase as fast with increasing W as when $W < x_M$. In the simulation and measurement results, the drop at $0.5\ \mu$m is not as sharp due to the limited resolution of the abscissa, which is always larger than the Debye length.[18]

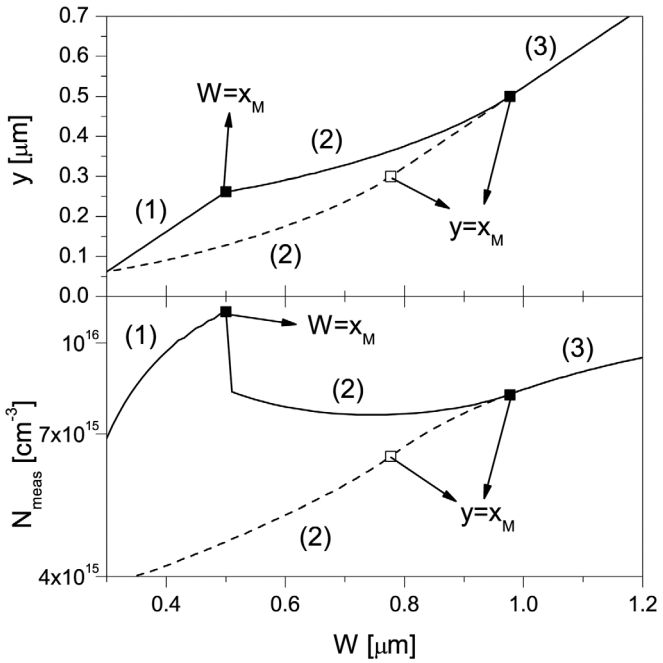

FIG. 7. Top Relation between the width y of the region where an acceptor defect density is charged and the depletion width W. Bottom: Relation between the apparent doping density N_{meas} and W. Solid curves: $V_{init} = -2\,\mathrm{V}$; dashed curves: $V_{init} = 0\,\mathrm{V}$. The squares indicate the points where $y = x_M$ and $W = x_M$ and thus where the equations used to calculate y and N_{meas} change. The regions that require different equations are marked. (1): $y < W < x_M$; (2): $y < x_M < W$; (3): $x_M < y < W$.

At large values of W ($W > 0.8\,\mu\mathrm{m}$), the curves for N_{meas} simulated at different initial voltages are horizontally shifted with respect to each other in Fig. 4. In this region, y and N_{meas} are calculated using Eqs. (12) and (13). Even though the value of E_F in the bulk of the absorber was assumed to be independent of V_{init} in all previous calculations, there is a slight interdependence. From the simulation results, one gets $E_F \approx 0.14\,\mathrm{eV}$ for $V_{init} = -2\,\mathrm{V}$ and $E_F \approx 0.17\,\mathrm{V}$ for $V_{init} = 0\,\mathrm{V}$. Using these values, one can calculate $k = W - y$, leading to $0.50\,\mu\mathrm{m}$ and $0.46\,\mu\mathrm{m}$, respectively. As shown in Fig. 6, k can easily be determined as the onset of the increase of N_{meas} when no metastable defect is present. When $N_M \neq 0$, however, the onset is no longer visible. It is obscured because Eqs. (16) and (17) are valid in this region. The different value of k can, however, still be determined at the point where $N_{meas} = N_A + N_t/2$. At this point, according to Eq. (13), $y/W = [0.5]$ and thus $W = 2\,k$. Hence, one can predict that $N_{meas} = N_A + N_t/2$ will approximately occur at $W = 0.92\,\mu\mathrm{m}$ for $V_{init} = 0\,\mathrm{V}$ and at $1.00\,\mu\mathrm{m}$ for $V_{init} = -2\,\mathrm{V}$. This prediction is indeed visible in Fig. 4, where these points are marked with a star.

SUMMARY AND CONCLUSIONS

We extended the thin film solar cell simulation software SCAPS to enable the simulation of metastabilities due to lattice relaxations in defects. The activation energies of the different processes involved are not independent as they have to obey to the principle of detailed balance. The calculation of the distribution over the different configurations of the defect has to be performed in an iterative way. When the defect density is high with respect to the shallow doping density, a clamping procedure is used to improve convergence of the algorithm.

The possibilities of this new facility have been applied to model the reverse bias metastability in CIGS based solar cells as a result of the presence of $(V_{Se}-V_{Cu})$ complexes. A fair agreement between measurement and simulation is found with an uncomplicated model. The influence of the $(V_{Se}-V_{Cu})$ complex on C-V-measurements for the reverse bias metastability can be explained by optimizing only five parameter values (E_{TR}, N_M, N_A, N_t, and E_t). Hence, this measurement in combination with simulations can be of help to determine these parameters. There are two specific features that appear in the apparent doping density curves after applying a reverse bias treatment to the sample: The appearance of a local maximum and a horizontal shift of the curve when the initial voltage gets more reverse. These features are a direct consequence of the fact that the region where the $(V_{Se}-V_{Cu})$ complexes are in their acceptor configuration is larger when V_{init} is more reverse.

ACKNOWLEDGMENTS

We acknowledge the support of the Research Foundation—Flanders (K.D., Ph.D. Fellowship). We thank N. Barreau (Université de Nantes) for providing the CIGS sample.

[1]M. Igalson, H. W. Schock, J. Appl. Phys. **80**, 5765 (1996).
[2]P. Zabierowski, U. Rau, and M. Igalson, Thin Solid Films, **387**, 147 (2001).
[3]J. T. Heath, J. D. Cohen, and W. N. Shafarman, J. Appl. Phys. **95**, 1000 (2004).
[4]P. Zabierowski, in: *Thin Film Solar Cells: Current Status and Future Trends*, edited by A. Bosio and A. Romeo (Nova Science Publishers, Hauppauge, NY, 2010).
[5]T. Meyer, F. Engelhardt, J. Parisi, and U. Rau, J. Appl. Phys. **91**, 5093 (2002).
[6]U. Rau, A. Jasenek, R. Herberholz, H. W. Schock, J. F. Guillemoles, D. Lincot, and L. Kronik, in: 2nd Conference on Photovoltaic Energy Conversion, E. C. Joint Res. Centre, Luxembourg, Wien, 1998, pp. 428–433.
[7]M. Burgelman, F. Engelhardt, J. F. Guillemoles, R. Herberholz, M. Igalson, R. Klenk, M. Lampert, T. Meyer, V. Nadenau, A. Niemegeers, J. Parisi, U. Rau, H. W. Schock, M. Schmitt, O. Seifert, T. Walter, and S. Zott, Prog. Photovoltaics **5**, 121 (1997).
[8]I. L. Eisgruber, J. E. Granata, J. R. Sites, J. Hou, and J. Kessler, Solar Energy Mater. Solar Cells **53**, 367 (1998).
[9]S. Lany and A. Zunger, J. Appl. Phys. **100**, 113725 (2006).
[10]S. Lany and A. Zunger, Phys. Rev. Lett. **100**, 016401 (2008).
[11]M. Igalson, P. Zabierowski, D. Przado, A. Urbaniak, M. Edoff, and W. N. Shafarman, Solar Energy Mater. Solar Cells **93**, 1290 (2009).
[12]M. Cwil, M. Igalson, P. Zabierowski, and S. Siebentritt, J. Appl. Phys. **103**, 063701 (2008).
[13]M. Burgelman, P. Nollet, and S. Degrave, Thin Solid Films **361**, 527 (2000).
[14]K. Decock S. Khelifi, and M. Burgelman, Thin Solid Films **519**, 7481 (2011).
[15]L. C. Kimerling, J. Appl. Phys. **45**, 1839 (1974).
[16]N. Barreau, J. Lahnemann, F. Couzinie-Devy, L. Assmann, P. Bertoncini, and J. Kessler, Solar Energy Mater. Solar Cells **93**, 2013 (2009).
[17]R. Scheer and H.-W. Schock, *Chalcogenide Photovoltaics* (Wiley-VCH, Weinheim, 2011).
[18]S. M. Sze and K. K. Ng, *Physics of Semiconductor Devices*, 3rd ed. (Wiley & Sons, Hoboken NJ, 2007).